

## Rayleigh-Bénard thermal convection perturbed by a horizontal heat flux

Jinzi Mac Huang<sup>1,2\*</sup> and Jun Zhang<sup>1,2,3†</sup>1. NYU-ECNU Institute of Physics and Institute of Mathematical Sciences,  
New York University Shanghai, Shanghai, 200122, China

2. Applied Math Lab, Courant Institute, New York University, New York, NY 10012, USA

3. Department of Physics, New York University, New York, NY 10012, USA

(Dated: September 11, 2022)

In Rayleigh-Bénard convection, it has been found that the amount of heat passing through the fluid has a power law dependence on the imposed temperature difference. Modifying this dependence, either enhancing or reducing the heat transfer capability of fluids, is important in many scientific and practical applications. We present a simple means to control the heat transfer in Rayleigh-Bénard convection by injecting heat through one side of the fluid domain and extracting the same amount of heat from the opposite side. This effective horizontal heat flux enhances the overall fluid circulation, and increases the heat transfer rate in the vertical direction. Our numerical and theoretical studies demonstrate how the classical Rayleigh-Bénard convection responds to such a perturbation, especially when the system is close to the onset of convection.

There are many similarities between thermal, fluid, and electronic systems. For example, Ohm's law relates a flux of charge to an electrostatic potential difference, while Fourier's law of heat conduction  $q \propto -\Delta T$  states that heat flux  $q$  is proportional to the temperature difference  $\Delta T$ . These similarities show the shared mathematical form of the conservation laws [1] regarding electrical charge, energy, and mass. Drawing analogies between these different systems has led to the advances of many mechanisms that are known in one system but not obvious in the other [2]. As an example, Nikola Tesla's concept of fluidic diode has recently been realized [3, 4], leading to the design of fluidic AC-to-DC rectifier.

Combining these systems also reveals nontrivial and surprising dynamics. For example, adding mass flow to a thermal system introduces nonlinearity that Fourier's law does not capture. Famously, thermal convection appears when a temperature gradient drives fluid motion [5, 6]. The canonical example here is the Rayleigh-Bénard convection, whose configuration is simple: a square domain of fluid is subject to heating from the bottom and cooling from the top, while the sidewalls remain adiabatic, as shown in Fig. 1. The low-temperature fluid near the top plate is heavier than the warm fluid near the bottom, which creates an instability under gravity. Thus convection occurs when this system is beyond a critical threshold, and the vertical heat flux has been observed to depend on the temperature difference nonlinearly:  $q \propto -\Delta T^a$  where an exponent  $a \approx 4/3$  is observed for a wide range of parameters [7, 8].

There have been numerous attempts to break this scaling, as a reduced or enhanced heat transfer rate is sometimes desired in applications like effective ventilation or energy preservation. Successful experimental examples include adding rotation to the Rayleigh-Bénard convection [9, 10], where moderate rotation rates enhance the

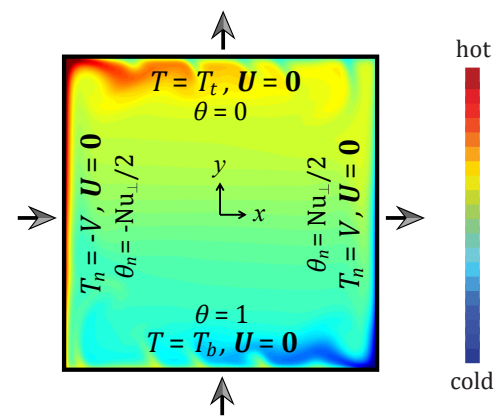


Figure 1. A square thermal convection cell of size  $L \times L$ . Temperatures  $T_t$  and  $T_b$  are fixed at the top and bottom, and temperature gradients  $-V$  and  $V$  are imposed at the left and right sidewalls ( $V = 0$  is the classical Rayleigh-Bénard convection). Simulation parameters here are  $Ra = 10^7$ ,  $Pr = 4.4$ ,  $Nu_{\perp} = 80$ .

bottom-top heat flux; changing the surface roughness of the top and bottom plates [11], where corrugated surface patterns result in higher heat transfer; and inserting insulating partitions into the fluid domain [12] which act as flow guides and lead to a higher overall heat transfer rate. Numerical studies have also shown the heat transfer rate to increase over time as an ice ceiling melts into the water below [13], and in general, a moving boundary enhances heat and mass transfer [14–16]. Beyond their potentially broad applications, such results can also help us better understand the complex coupling between heat and fluid.

Here, we impose a horizontal heat flux to the classical Rayleigh-Bénard convection as shown in Fig. 1, where the sidewalls are no longer adiabatic but  $|V| > 0$ . These vertical heating/cooling walls induce additional fluid motion and lead to the formation of upward/downward buoyancy jets. These jets can, in principle, enhance bulk mixing

\* machuang@nyu.edu

† jz11@nyu.edu

and improve the vertical heat transfer. We next investigate this configuration systematically through 2D numerical simulations, considering that the flow and heat structures involved that are largely 2D and the heat transfer properties of Rayleigh-Bénard convection can be faithfully recovered in 2D numerical simulations [8, 17, 18].

*The model.*— To formulate our problem dimensionlessly, we rescale temperature by  $\Delta T = T_b - T_t$ , rescale length by  $L/2$  (half the domain height) so the coordinates  $(x, y) \in \Omega \triangleq (-1, 1) \times (-1, 1)$ , and rescale time by the thermal diffusion time scale of  $L^2/4\kappa$  where  $\kappa$  is the thermal diffusivity of the fluid. The dimensionless velocity field is then  $\mathbf{u} = UL/2\kappa$  and the dimensionless temperature is  $\theta = (T - T_t)/\Delta T$ . Two relevant dimensionless numbers are the Rayleigh number  $\text{Ra} = \alpha g \Delta T L^3 / \kappa \nu$  which measures the relative strength between the thermally induced buoyancy force and the fluid viscous force, and the Prandtl number  $\text{Pr} = \nu / \kappa$  which is the ratio between fluid viscosity and thermal diffusivity. Here  $\rho, \nu, \alpha$  and  $g$  are the density, kinematic viscosity, and thermal expansion coefficient of the fluid and the acceleration due to gravity, respectively.

The heat flux passing through the vertical direction can be non-dimensionalized as the Nusselt number,  $\text{Nu} = q/q_c = \int_{-1}^1 \partial_y \theta(x, 1) dx$ , which is the ratio between the convective flux  $q = (K/L) \int_0^L \partial_Y T(X, L) dX$  and the conductive flux  $q_c = (K/L) \Delta T$ . Here,  $K$  is the thermal conductivity. To simplify our notation, we also define a horizontal Nusselt number as  $\text{Nu}_\perp = VL/\Delta T$ . The symbol  $\perp$  is used to indicate that the horizontal heat flux is perpendicular to the traditionally vertical heat flux (Nu) in Rayleigh-Bénard convection. Naturally, this is a dimensionless measure of the imposed horizontal flux. Another important number is the Reynolds number  $\text{Re} = U_{\text{max}} L / \nu = 2\text{Pr}^{-1} u_{\text{max}}$ , where the maximum velocity  $u_{\text{max}} = \max |\mathbf{u}|$  represents the speed scale.

Overall, the system has three control parameters, or *inputs*: Ra, Pr and  $\text{Nu}_\perp$ . *Outputs* like Nu, Re are functions of these inputs. To further simplify our study, we set  $\text{Pr} = 4.4$  (water at 40°C) for all the simulations.

Denoting the vorticity as  $\omega = \hat{\mathbf{k}} \cdot \nabla \times \mathbf{u}$  and the stream function as  $\psi$  such that  $\mathbf{u} = \nabla_\perp \psi = (\psi_y, -\psi_x)$ , we can write the Navier-Stokes equation in the vorticity-stream function format

$$\frac{\partial \theta}{\partial t} + \mathbf{u} \cdot \nabla \theta = \Delta \theta \quad \text{in } \Omega, \quad (1)$$

$$\frac{\partial \omega}{\partial t} + \mathbf{u} \cdot \nabla \omega = \text{Pr} \Delta \omega + \frac{1}{8} \text{Pr} \text{Ra} \frac{\partial \theta}{\partial x} \quad \text{in } \Omega, \quad (2)$$

$$-\Delta \psi = \omega, \quad \mathbf{u} = \nabla_\perp \psi \quad \text{in } \Omega, \quad (3)$$

with boundary conditions

$$\left\{ \begin{array}{l} \psi = \psi_n = 0 \quad \text{on } \partial\Omega, \\ \theta = 0 \quad \text{on } \partial\Omega_{\text{up}}, \quad \theta = 1 \quad \text{on } \partial\Omega_{\text{down}}, \\ \frac{\partial \theta}{\partial n} = -\frac{1}{2} \text{Nu}_\perp \quad \text{on } \partial\Omega_{\text{left}}, \quad \frac{\partial \theta}{\partial n} = \frac{1}{2} \text{Nu}_\perp \quad \text{on } \partial\Omega_{\text{right}}. \end{array} \right.$$

To solve these equations, we employ a pseudo-spectral scheme [19] that uses the Chebyshev method. Spatial variables are discretized on the Chebyshev nodes, with operations like derivatives and integrations performed through corresponding discrete operators. At each timestep, a second-order implicit Backward-Differentiation method solves for the stiff parabolic equations and the nonlinear equations are handled by the preconditioned Minimal Residual method. Typically, the simulation has 300 Chebyshev nodes in each dimension, and the timestep is set as  $\Delta t \propto \text{Ra}^{-1/2}$  (as  $|\mathbf{u}| \propto \text{Ra}^{1/2}$  [8]) to maintain accuracy and rapid convergence of the nonlinear solver.

*Results.*—The effect of adding horizontal heat flux to Rayleigh-Bénard convection is directly reflected in the temperature and flow fields. Figure 2(a)-(b) shows two time-averaged profiles at different magnitudes of horizontal flux. At a constant  $\text{Ra} = 1.25 \times 10^4$ , the Nusselt number for the classical Rayleigh-Bénard convection ( $\text{Nu}_\perp = 0$ ) is  $\text{Nu}_0 \approx 2.4$ , and the direction of circulation is not deterministic. A clear influence of the horizontal flux is already present at  $\text{Nu}_\perp = 1/4$ , where the direction of circulation becomes deterministically clockwise with the aid of buoyancy driven flows near the vertical walls. At  $\text{Nu}_\perp = 16$ , the profiles of temperature and flow fields are dictated by the sidewall heating and cooling, similar to the profiles in a horizontal thermal convection without bottom heating or top cooling [20]. With increasing  $\text{Nu}_\perp$  both the circulation velocity and the Reynolds number increase, as shown in Fig. 2(a)-(b) and (g).

The temperature distributions along the horizontal center line  $y = 0$  and the vertical center line  $x = 0$  are shown in Fig. 2(c)-(d). On the horizontal cut  $y = 0$ , the temperature stays at  $\theta(x, 0) = 0.5$  when no horizontal flux is added. As the sidewall heating-cooling increases, the temperature on the heating wall becomes higher while the temperature on the cooling wall becomes symmetrically lower. This change of temperature generates buoyancy jets along the two sidewalls, which can also be seen in Fig. 2(a)-(b). Due to flow advection, two thermal boundary layers develop near the sidewalls, similar to the boundary layer profile near a vertical heated or cooled wall in an infinite space [21]. As the buoyancy jets move upward/downward, they are diverted to the right/left as they meet the top/bottom wall, resulting in an overall clockwise circulation. Due to the relatively hot/cold fluid coming from the region near the left/right wall, the vertical temperature profile  $\theta(0, y)$  in Fig. 2(d) has an inversion with a temperature rise near the top wall and a drop near the bottom. Remarkably, the magnitude of the temperature gradient near the top and bottom wall is increased, leading to a higher vertical heat transfer rate.

Defining  $\theta_l = \theta(-1, 0)$ ,  $\theta_r = \theta(1, 0)$ , and  $\theta_c = \theta(0, 0)$  to be the temperature of the left wall, right wall, and bulk center, their time-averaged values at different  $\text{Nu}_\perp$  are shown in Fig. 2(e). The temperature rise and drop of the left and right wall are symmetric with respect to

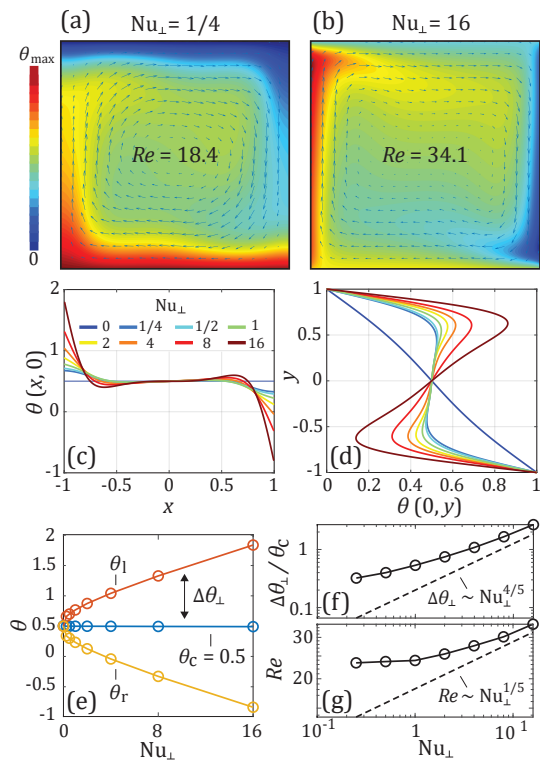


Figure 2. Flow and temperature profiles of Rayleigh-Bénard convection with an additional horizontal heat flux. (a)-(b) Time averaged flow and temperature fields at  $Ra = 1.25 \times 10^4$  with two different strength of horizontal flux. (c) Horizontal temperature profiles along  $y = 0$ . (d) Vertical temperature profiles along  $x = 0$ . (e) The time-averaged left wall temperature  $\theta_l$  increases while the right wall temperature  $\theta_r$  decreases symmetrically with increasing  $Nu_{\perp}$ . (f) At high  $Nu_{\perp}$ , the horizontal temperature change  $\Delta\theta_{\perp} = \theta_l - \theta_c = \theta_c - \theta_r$  takes the  $4/5$  power law as an asymptote. (g) the Reynolds number  $Re = 2Pr^{-1}u_{\max}$  also approaches the power law  $Re \sim Nu_{\perp}^{1/5}$ .

the bulk center, which has a mean temperature  $\theta_c = 0.5$ . Defining  $\Delta\theta_{\perp} = \theta_l - \theta_c = \theta_c - \theta_r$  to be the temperature change on the sidewall, it increases with the horizontal flux  $Nu_{\perp}$  as shown in Fig. 2(f). Asymptotically, the measured data approaches  $\Delta\theta_{\perp} \propto Nu_{\perp}^{4/5}$  when the side heating becomes dominant. This is consistent with the boundary layer scaling between the temperature rise  $\Delta T_{\perp}$  and the injected heat  $Q$  from a vertical heated wall,  $\Delta T_{\perp} \propto Q^{4/5}$  [21]. Moreover, the Reynolds number near the vertical heated wall also approaches the scaling  $Re \propto \Delta T_{\perp}^{1/4} \propto Q^{1/5}$  as shown in Fig. 2(g), consistent with the boundary layer theory [21].

We next examine the vertical heat transfer capability measured by the Nusselt number  $Nu$ . Without the horizontal flux ( $Nu_{\perp} = 0$ ),  $Nu_0 = Nu|_{Nu_{\perp}=0}$  is known to depend on the Rayleigh number  $Ra$  in a nonlinear way: When the Rayleigh number is below a critical number (around 1708 [22]), the viscous force suppresses fluid motion and the fluid behaves like solid, hence  $Nu_0 = 1$ ; Increasing the Rayleigh number beyond critical, a power

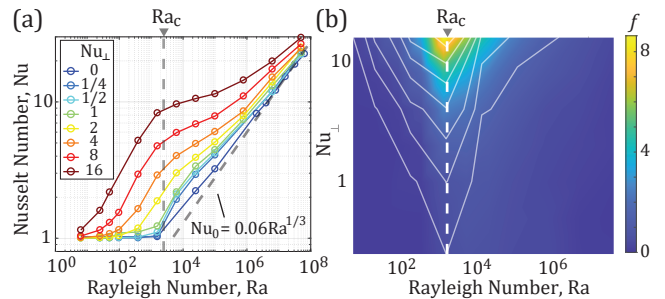


Figure 3. Nusselt number  $Nu$  depends on the Rayleigh number  $Ra$  and the horizontal heat flux  $Nu_{\perp}$ . (a) The Nusselt number increases with  $Nu_{\perp}$  at a given  $Ra$ . The blue curve  $Nu_0$  corresponds to the classic Rayleigh-Bénard convection with adiabatic sidewalls. (b) The relative  $Nu$  enhancement  $f = (Nu/Nu_0) - 1$  increases with  $Nu_{\perp}$ . At any given  $Nu_{\perp}$ ,  $f$  reaches a local maximum near  $Ra_c = 2415$ . The color map presents the smoothed value of  $f$  through interpolation, and white contour lines show the raw data from (a).

law relation emerges as  $Nu_0 \propto Ra^{1/3}$ , despite local deviations [8]. In our simulation, this relation is recovered as the blue data of Fig. 3(a). As we shall determine later, the critical Rayleigh number in our numerical system is near  $Ra_c = 2415$ , slightly higher than the theoretical value [22], likely due to the finite resolution set by the numerical method.

The behavior near  $Ra_c$  changes with the addition of a horizontal flux: Figure 3(a) shows that the Nusselt number can be greater than 1 even when  $Ra < Ra_c$ . One explanation is that the side heating and cooling set up the large scale circulation even though the vertical temperature gradient is small, and this mixing effectively stirs the bulk fluid and increases the vertical flux. More precisely, the warm fluid close to the left wall flows upward to the top plate, creating a larger temperature difference between the fluid and the top plate and a smaller characteristic length as the boundary layer thickness decreases with the fluid velocity [Fig. 2(d)]. All together, these effects result in a larger temperature gradient near the top plate hence an enhanced  $Nu$ . Similar analysis can be performed symmetrically near the bottom plate, as the system is symmetric to its center such that  $\theta(x, y) = 1 - \theta(-x, -y)$ .

This enhancement of  $Nu$  exists for a wide range of  $Ra$  and  $Nu_{\perp}$ . Shown in Fig. 3(b), the relative enhancement  $f(Ra, Nu_{\perp}) = (Nu/Nu_0) - 1$  is an increasing function of the horizontal flux  $Nu_{\perp}$  when  $Ra$  is fixed. At a fixed  $Nu_{\perp}$ , however, the value of  $f$  peaks around the critical Rayleigh number  $Ra_c$ . One possible explanation for this peak is that the fluid (and hence the vertical heat flux) is easily perturbed when  $Ra \sim Ra_c$  while the unperturbed  $Nu_0$  is still at unity.

As  $Ra$  increases, the relative enhancement  $f$  becomes smaller and approaches 0 asymptotically. This is understandable as the relative strength of the imposed horizontal flux and the unperturbed vertical flux  $Nu_{\perp}/Nu_0$

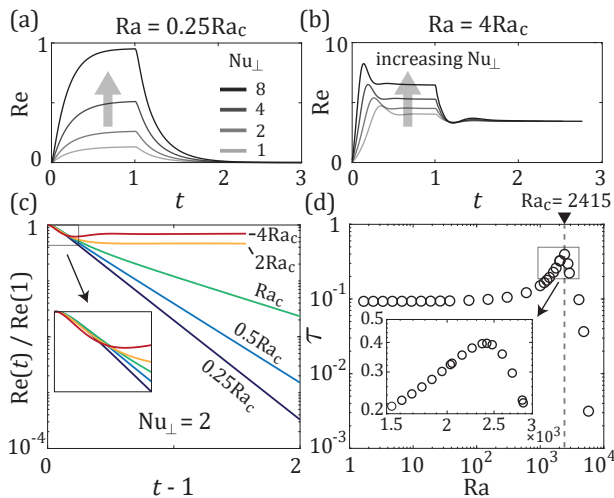


Figure 4. Rayleigh-Bénard convection perturbed by a transient horizontal flux. An imposed horizontal flux during  $t \in (0, 1)$  is removed after  $t = 1$ , allowing the system to relax back to the classical Rayleigh-Bénard convection. (a) Reynolds number increases in below-critical Rayleigh-Bénard convection when a horizontal flux is added, and fluid motion diminishes after this flux is removed. (b) Reynolds number in the above-critical system decreases to the usual level of Rayleigh-Bénard convection after the perturbation is removed. (c) The fluid motion decays exponentially in the below-critical Rayleigh-Bénard convection after the perturbation is removed. (d) The relaxation time  $\tau$  reaches a maximum at  $Ra_c = 2415$ , approaches a constant as  $Ra \rightarrow 0$ , and decreases rapidly when  $Ra > Ra_c$ .  $Nu_{\perp} = 2$  in (c)-(d), other  $Nu_{\perp}$  presents similar dynamics and decay rate.

diminishes with increasing  $Ra$ . Eventually,  $Nu_0 \gg Nu_{\perp}$  as  $Ra \rightarrow \infty$  so the horizontal flux has negligible effects on the Rayleigh-Bénard convection.

In the following examples, we impose a horizontal heat flux during the time  $t \in (0, 1)$ , and then turn it off at  $t = 1$  so the system can return to the configuration of classical Rayleigh-Bénard convection. Figure 4(a)-(b) shows the fluid response to such perturbations. The Reynolds number for both the below-critical [ $Ra < Ra_c$ , Fig. 4(a)] and above-critical [ $Ra > Ra_c$ , Fig. 4(b)] states increases while the horizontal flux is applied. This is expected as there is a horizontal temperature difference in the fluid, which results in convective motion without threshold.

When the horizontal flux is turned off, the flow speed, represented by the Reynolds number  $Re(t)$ , relaxes to that of Rayleigh-Bénard convection: In Fig. 4(a), the flow velocity drops to 0 as the system is below-critical; in Fig. 4(b), the flow velocity decreases to a non-vanishing value  $Re(\infty)$  as the system is convective.

To assess how fast the system relaxes to its equilibrium state, we define a relaxation time  $\tau$  through  $Re(1) - Re(\tau) = e^{-1}[Re(1) - Re(\infty)]$ , whose dependence on  $Ra$  is shown in Fig. 4(d). Just like the dynamical transition shown in Fig. 3,  $\tau$  behaves non-smoothly when

$Ra$  crosses a critical value, which can be identified as  $Ra_c = 2415$  in Fig. 4(d). Near  $Ra_c$ , a peak of relaxation time  $\tau$  appears, suggesting a critical slowing down [23]. This can also be seen in the inset of Fig. 4(c), where the  $Ra = Ra_c$  curve (green) decays the slowest. It is worth noting that, at the same  $Ra_c$ , the Nusselt enhancement  $f$  also reaches a maximum when holding  $Nu_{\perp}$  constant [Fig. 3(b)].

In the below-critical system, the relaxation of temperature and flow fields is closely associated with the dissipation of energy through the diffusion of heat and momentum. In the extreme case of  $Ra \rightarrow 0$ , the flow speed is almost 0 and Eq. (1) becomes the heat equation,  $\partial\theta/\partial t = \Delta\theta$ , whose solution decays exponentially in time. The relaxation time of this exponential decay is set by the initial condition of  $\theta$  and geometry, therefore independent of  $Ra$ . As the flow field is only driven by the temperature field, it shall exhibit the same decay in time. This confirms the exponential decay in Fig. 4(c), and explains why the relaxation time  $\tau$  in Fig. 4(d) is almost constant for small  $Ra$ . In that case, the dimensional relaxation time  $T_{\tau} = L^2\tau/4\kappa$  is an increasing function of the system size  $L$  and a decreasing function of the thermal conductivity  $\kappa$ .

Above  $Ra_c$ , the relaxation time in Fig. 4(d) decreases rapidly with  $Ra$ , as the vertical temperature gradient sustains fluid motion and the perturbation applied during  $t \in (0, 1)$  is quickly “washed away”.

*Discussion.*—In this work, we numerically explore the effect of an additional horizontal heat flux in Rayleigh-Bénard convection. As expected, this horizontal heat flux induces fluid motion, enhances large scale circulation, and increases the Nusselt number. We observed a monotonic response in vertical heat flux when the horizontal heat flux is added, and this allows us to directly control the vertical heat transfer rate. This mechanism could prove useful in engineering applications—for example to control environments like cooling towers, where the addition of heating and cooling pads on sidewalls could increase the overall cooling rate. On a larger scale, the ground is warmer than the surrounding air during the day time, hence the addition of vertical heating and cooling sources could even lower the near-ground temperature.

By perturbing Rayleigh-Bénard convection near its critical state, we also observe a critical slowing down where the thermo-fluid system presents significant *inertia*—any perturbation to the flow or temperature field decays at the slowest rate. Also, the configuration of perturbed Rayleigh-Bénard convection allows us to control one flux with the other—much similar to the electronic transistors. This *thermal transistor* thus responds to the *signal* ( $Nu_{\perp}$ ) more rapidly with increasing  $Ra$ , but has a slow relaxation when  $Ra$  is low. Right at  $Ra_c$ , any *signal* would have the longest influence to the conductivity ( $Nu$ ) of *thermal transistor* and the highest amplification ratio  $f$  is also reached. These nonlinear, hysteretic behaviors of *thermal transistor*, could have future applications in the design of “thermal circuits”.

- 
- [1] L. C. Evans, *Partial Differential Equations*, Graduate studies in mathematics (American Mathematical Society, 2010).
- [2] J. C. Schönfeld, Analogy of hydraulic, mechanical, acoustic and electric systems, Applied Scientific Research, Section A **3**, 417 (1954).
- [3] Q. M. Nguyen, J. Abouezzi, and L. Ristroph, Early turbulence and pulsatile flows enhance diodicity of Tesla's macrofluidic valve, Nature Communications **12**, 1 (2021).
- [4] Q. M. Nguyen, D. Huang, E. Zauderer, G. Romanelli, C. L. Meyer, and L. Ristroph, Tesla's fluidic diode and the electronic-hydraulic analogy, American Journal of Physics **89**, 393 (2021).
- [5] J. Niemela, L. Skrbek, K. Sreenivasan, and R. Donnelly, Turbulent convection at very high Rayleigh numbers, Nature **404**, 837 (2000).
- [6] S. Childress, *An Introduction to Theoretical Fluid Mechanics*, Courant lecture notes in mathematics (Courant Institute of Mathematical Sciences, 2009).
- [7] A. Belmonte, A. Tilgner, and A. Libchaber, Temperature and velocity boundary layers in turbulent convection, Physical Review E **50**, 269 (1994).
- [8] G. Ahlers, S. Grossmann, and D. Lohse, Heat transfer and large scale dynamics in turbulent Rayleigh-Bénard convection, Rev. Mod. Phys. **81**, 503 (2009).
- [9] R. J. A. M. Stevens, J.-Q. Zhong, H. J. H. Clercx, G. Ahlers, and D. Lohse, Transitions between turbulent states in rotating Rayleigh-Bénard convection, Phys. Rev. Lett. **103**, 024503 (2009).
- [10] J.-Q. Zhong and G. Ahlers, Heat transport and the large-scale circulation in rotating turbulent Rayleigh-Bénard convection, J. Fluid Mech. **665**, 300 (2010).
- [11] Y.-B. Du and P. Tong, Enhanced heat transport in turbulent convection over a rough surface, Phys. Rev. Lett. **81**, 987 (1998).
- [12] Y. Bao, J. Chen, B.-F. Liu, Z.-S. She, J. Zhang, and Q. Zhou, Enhanced heat transport in partitioned thermal convection, J. Fluid Mech. **784**, 10.1017/jfm.2015.610 (2015).
- [13] B. Favier, J. Purseed, and L. Duchemin, Rayleigh-Bénard convection with a melting boundary, J. Fluid Mech. **858**, 437 (2019).
- [14] M. S. D. Wykes, J. M. Huang, G. A. Hajjar, and L. Ristroph, Self-sculpting of a dissolvable body due to gravitational convection, Phys. Rev. Fluids **3**, 043801 (2018).
- [15] J. M. Huang, J. Tong, M. Shelley, and L. Ristroph, Ultra-sharp pinnacles sculpted by natural convective dissolution, Proc. Natl. Acad. Sci. **117**, 23339 (2020).
- [16] J. M. Huang, M. J. Shelley, and D. B. Stein, A stable and accurate scheme for solving the Stefan problem coupled with natural convection using the Immersed Boundary Smooth Extension method, J. Comput. Phys. , 110162 (2021).
- [17] J. Schmalzl, M. Breuer, and U. Hansen, The influence of the Prandtl number on the style of vigorous thermal convection, Geophysical & Astrophysical Fluid Dynamics **96**, 381 (2002).
- [18] J. Schmalzl, M. Breuer, and U. Hansen, On the validity of two-dimensional numerical approaches to time-dependent thermal convection, EPL (Europhysics Letters) **67**, 390 (2004).
- [19] R. Peyret, *Spectral Methods for Incompressible Viscous Flow*, Applied Mathematical Sciences (Springer New York, 2002).
- [20] A. Belmonte, A. Tilgner, and A. Libchaber, Turbulence and internal waves in side-heated convection, Phys. Rev. E **51**, 5681 (1995).
- [21] H. Schlichting and K. Gersten, *Boundary-Layer Theory* (Springer Berlin Heidelberg, 2016).
- [22] E. L. Koschmieder, *Bénard cells and Taylor vortices* (Cambridge University Press, 1993).
- [23] P. C. Hohenberg and B. I. Halperin, Theory of dynamic critical phenomena, Rev. Mod. Phys. **49**, 435 (1977).